

Control and performance assessment of grid-connected PMSG-based wind turbine equipped with diode bridge rectifier and boost converter using three different control strategies

Yahya Abdollahi¹, Mohsen rahimi^{*2}, Abolfazl Halvaei-Niasar³

^{1,2,3} Department of Electrical and Computer Engineering, University of Kashan, Kashan, Iran

^{1,2,3} P. O. BOX: 87317-53153

Email: *mrahimi@kashanu.ac.ir

Abstract

In this paper, as the main contribution, three sensorless control structures are presented for the control of the grid-connected PMSG-based wind turbine (WT) employing boost converter and diode rectifier as the machine-side converter. Then, detailed control structures of the boost converter and grid-side converter at the three mentioned control strategies are extracted, and next, features of the abovementioned control strategies are investigated and compared against wind speed variation and grid voltage dip. The boost converter, in the first control strategy, controls the generator speed at the MPPT mode, and in the second control strategy, it regulates the PMSG active power to its set point value. Also, the boost converter, in the third control strategy, adjusts the voltage of the dc link capacitor to its set point value. In this paper, steady-state performance and transient/LVRT behavior of the WT system are examined for each mentioned control strategy in the Matlab-Simulink environment. It is shown that WT steady-state responses are relatively identical for all three control strategies. However, as an interesting result, at the fault conditions, the third control strategy has superior performance, and thus, the WT fault ride-through behavior enhances significantly with the third control structure without any hardware protection.

Keywords: PMSG-based wind turbine, boost converter, machine-side converter, sensorless control strategies, transient and LVRT behavior

1. Introduction

Currently, full converter-based WTs with permanent magnet synchronous generators (PMSGs), known as PMSG-based WTs, are widely used in wind turbine industry and grid-connected applications.

PMSG-based WTs have substantial advantages such as simple structure, enhanced power factor, lower maintenance cost and wider speed range in maximum power operation mode [1-5].

PMSG-based WTs are attached to the grid via cascaded power electronics converters, called machine and grid side converters (MSC and GSC). Considering the MSC structure, in PMSG-based WTs, the MSC can be a voltage source converter (VSC) [6-7] or combination of the boost converter and diode-rectifier can be used as the MSC [8-10]. Numerous papers have discussed about the control and performance analysis of the PMSG-WTs with back-to-back frequency converters. A number of papers have also dealt with the behavior analysis and control of PMSG-WTS employing combination of boost converter and diode-rectifier as the MSC [8-24].

In [8], PMSG-WT stability and impact of speed controller parameters on the WT stability is studied by the modal analysis. Ref [9] focuses on studying the oscillation modes of direct driven PMSGs connected to the power grid by developing small signal models of PMSG-based WTGS with different converter topologies. In [10], it is dealt with the modification of the boost converter control for improving the PMSG-WT performance. Refs. [11-13] discusses regarding the sensorless performance of small PMSG-WTs with diode bridge rectifier in the maximum power mode. In [14], a maximum power mode approach, known as incremental conductance approach, is presented for small PMSG-WT supplying a dc-load. In [15], sliding mode control with improving transient approach is suggested for the PMSG-based WT control, in which diode rectifier, boost converter, neutral point clamped (NPC) inverter and L-filter are used as the interface between the wind turbine and grid. In [16], second-order sliding mode control are designed as voltage regulators for generating the control signal to bring the system to optimal boost converter voltage for realizing MPPT. In [17], power control of 5-phase PMSG-diode rectifier set associated to 3-interleaved Boost converter is investigated, and in [18-21], model predictive control are used for the PMSG-based WT control assisted with boost converter and diode rectifier. In [22-24], PMSG-WT supported by the boost converter is used for supplying stand-alone load. Ref [25] proposes three topologies of single-stage three-phase ac–dc buck–boost converters suitable for medium-voltage and high-power wind energy conversion systems that reduce the voltage and current stresses on the self-commutated switching device compared to existing solutions.

Usually, grid-connected PMSG-WTs are controlled based on two control structures, where in the first control structure [7-10, 26-29], the MSC adjusts the generator speed and the GSC sets the dc-link voltage, and, in the second control structure [6, 30-35], the MSC controls the voltage of the dc link capacitor and the GSC regulates the injected power to the grid.

The subject of this paper is about the control and performance analysis of the PMSG-WT implementing boost converter as the MSC, as depicted in Fig. 1. This research is a continuation of the previous papers [8, 10], where in both [8] and [10], the PMSG-WT uses boost converter and diode-rectifier and WT is controlled based on the first control structure, in which the boost converter adjusts the generator speed to a value corresponding to maximum power point tracking (MPPT) mode. In [8], small-signal stability analysis of the PMSG-WT is presented and impact of the speed controller parameters on the WT stability is investigated by the modal analysis. Also, in [10] modification of the control system of the boost converter for improving the PMSG-WT performance is presented.

In this paper, as the main contribution, three sensorless control structures are presented for the control of the PMSG-WT employing boost converter and diode-rectifier as the machine converter, and then responses of the mentioned control strategies are compared. In this way, first, the relationship between the active component of the stator current and boost converter current is extracted, and then a simple and efficient approach is presented for the generator speed estimation. Next, detailed control structures of the converters at the three mentioned control strategies are extracted and given. In the first control strategy, the boost converter is responsible for the control of the generator speed at the MPPT mode and GSC is used for regulation of the dc link voltage. In the second control strategy, the boost converter is used to set the PMSG active power at the reference value, and GSC adjusts the dc link voltage to its reference value. In the third control strategy, the boost converter regulates the dc link voltage at the reference value, and GSC controls the injected active power to the grid to a reference value corresponding to the MPPT mode. In the paper, steady-state performance and transient/LVRT behavior of the WT system are examined for each mentioned control strategy. It is shown that WT steady-state responses are relatively identical for all three control strategies. However, at the fault conditions, the third control strategy has better performance, and thus, the WT low voltage ride-through behavior improves significantly by using the third control structure without any hardware protection.

The paper is organized as follows. In Sections 2 and 3, mathematical modeling, current control and steady-state behavior of the study system are presented. In Section 4, three strategies are presented for the PMSG-WT control, and then, control loops of the boost converter and grid-side converter are extracted in each control strategy. Finally, in Section 5, time domain simulation results are given, and steady-state and transient capabilities of the three presented control strategies are compared and investigated.

2. Mathematical representation of the PMSG with diode rectifier

This section presents dynamic modeling of the PMSG and current control of the boost converter and GSC. In this study, for the PMSG modeling, the stator currents direction is considered into the stator windings.

The stator voltages and fluxes of a cylindrical pole PMSG, in the rotor dq reference frame with rotational speed of ω_r , can be given as [9]:

$$v_{dq} = R_s i_{dq} + j \omega_r \psi_{dq} + \frac{d\psi_{dq}}{dt} \quad (1)$$

$$\begin{cases} \psi_d = L_s i_d + \psi_{PM} \\ \psi_q = L_s i_q \end{cases} \quad (2)$$

where v , i and ψ stand for the stator voltage, current and flux, ψ_{pm} is the stator flux linkage due to rotor permanent magnet, R_s is the stator resistance, and L_s is the stator synchronous inductance. Also, ω_r is the rotor rotational speed, that at steady-state conditions is identical to the stator frequency, ω_s . Besides, the generator electromechanical torque in a cylindrical pole PMSG is given by

$$T_e = \frac{3}{2} \frac{p}{2} (\psi_{PM} i_{sq}) \quad (3)$$

where p denotes the number of generator poles.

2.1 Current control of boost converter

In Fig. 1, the boost converter is interfaced between the diode rectifier and grid-side converter, and by varying the duty cycle of the switch Q, the inductor current i_b can be controlled. Considering the current continuous mode (CCM) operation of the boost converter, two different cases related to *on* and *off* states of the switch Q can be considered. The boost converter average model over one switching cycle is achieved, as given in Fig. 2.

From Fig. 2, the dynamics of the boost converter current is achieved as

$$v_d = R_b i_b + L_b \frac{di_b}{dt} + v_{dc} (1-d) \quad (4)$$

where d denotes the switch Q duty cycle. Considering $d = d_0 + \Delta d$, $v_d = v_{d0} + \Delta v_d$, $i_b = i_{b0} + \Delta i_b$, and $v_{dc} = v_{dc0} + \Delta v_{dc}$, the small-signal model of the boost converter current dynamics is obtained as

given in (5), where the symbols Δ and 0 represent the small-signal variation, and operating point, respectively.

$$L_b \frac{d\Delta i_b}{dt} + R_b \Delta i_b = \Delta d v_{dc0} - \Delta v_{dc} (1 - d_0) + \Delta v_d \quad (5)$$

From (5) and by considering the boost converter controller as the PI type, the current control loop of the boost converter is obtained as given in Fig. 3, where the control signal d regulates i_b to its set point value.

By implementing the pole-zero deletion approach in Fig. 3, we have $k_p/k_i = R_b/L_b$, and by choosing $k_p = \alpha_b L_b$, the transfer function from i_{b-ref} to i_b is achieved as

$$\frac{i_b(s)}{i_b(s)^*} = \frac{\alpha_b}{s + \alpha_b} \quad (6)$$

where α_b denotes the current control closed loop bandwidth, which is selected sufficiently smaller than the converter switching frequency ω_{sw} .

2.2 Current control of the GSC

The GSC, in Fig. 1, is linked to the grid through interfaced passive filter and step-up transformer, where the filter and transformer are specified by inductance L_f and resistance R_f . The dynamics of the GSC current, in pu, is given by

$$v_{GSCdq} = R_f i_{gdq} + j\omega L_f i_{gdq} + \frac{L_f}{\omega_b} \frac{di_{gdq}}{dt} + v_{gdq} \quad (7)$$

where v_{GSCdq} , i_{gdq} and v_{gdq} are the dq-components of the GSC output voltage and current and grid voltage, respectively. Figure 4 shows the control loops of the GSC dq axes currents.

The GSC is normally controlled in the dq frame with the grid voltage orientation (GVO), in which $v_{gd} = |v_g|$, and $v_{gq} = 0$. In GVO, i_{gd} is the active power part of the GSC current used for regulation of the output active power or dc-link voltage.

Considering the WT control strategy, the GSC may regulate the dc-link voltage or the active power injected to the grid, and thus i_{gd}^* is achieved from the outer dc-link voltage control loop or outer active power control loop, as will be given in Section 4. Also, in the GVO reference frame, i_{gq} is the reactive power component of the GSC current used for the reactive power/grid voltage control.

3. Steady state behavior of the PMSG-WT with boost converter and diode rectifier

By equating the stator flux derivative to zero and from (1) and (2), the steady-state model of the surface mounted PMSG is achieved as given in (8).

$$v_{sdq} = R_s i_{sdq} + jX_s i_{sdq} + j\omega_r \psi_{pm} \quad (8)$$

Considering (8), Fig. 5, depicts the one-phase circuit of the PMSG at steady-state conditions, where $E_g = j\omega_r \psi_{pm}$ is the back-emf voltage of the stator, and X_s is the PMSG synchronous reactance.

In the study system of Fig. 1, the inductor L_b is selected such that the boost converter works at the continuous conduction mode (CCM). Hence, as depicted in Fig. 6, the boost converter at steady state conditions is modeled as a current source at the output of the diode-rectifier.

In Fig. 6, E_{abcg} and V_d are the three-phase back-emf voltages, and rectifier output voltage. By ignoring the stator resistance and according to [36], the rectifier average output voltage may be given as:

$$v_d = \frac{3\sqrt{3}}{\pi} |E_g| - \frac{3}{\pi} X_s i_b \quad (9)$$

where the second term in (9), i.e. $(3/\pi)X_s i_b$, is the voltage drop at the rectifier output due to synchronous reactance X_s . It is noted that due to reactance X_s , the current commutation in the diode rectifier is not instantaneous causing rectifier output voltage drop.

From (8) and Fig. 5 and by ignoring the stator resistance, the PMSG output active power can be given by

$$P_s = -\frac{3}{2} |E_g| i_{sq} = -\frac{3}{2} \omega_r \psi_{pm} i_{sq} \quad (10)$$

Because of presence of diode-rectifier, three-phase stator currents comprise higher harmonics, where in the synchronous reference frame, the stator currents with the fundamental frequency become dc terms and other harmonics appear as ripples with frequency of $6\omega_0$ (ω_0 is the fundamental frequency).

Hence, the fundamental part of the stator current and accordingly the average component of the q-axis stator current \bar{i}_{sq} are responsible for delivering the PMSG active power. Therefore, the average output active power of the PMSG can be given by

$$\bar{P}_s = -\frac{3}{2} |E_g| \bar{i}_{sq} = -\frac{3}{2} \omega_r \psi_{pm} \bar{i}_{sq} \quad (11)$$

where the superscript $-$ in (11) denotes the average value. In Fig. 6, by neglecting the rectifier losses and equating the average output powers of the PMSG and rectifier, we have:

$$-\frac{3}{2}|E_g|\bar{i}_{sq} = \left(\frac{3\sqrt{3}}{\pi}|E_g| - \frac{3}{\pi}X_s i_b \right) i_b \quad (12)$$

Simulation studies show that at different wind speeds, the term $(3/\pi)X_s i_b$ at the right side of (12) is a fraction of $(3\sqrt{3}/\pi)|E_g|$, so that at low wind speeds (about 6 m/s) this ratio is about 0.01 and at nominal wind speeds, this ratio is about 0.1. Given this fact, (8) can be rewritten as

$$-\frac{3}{2}|E_g|\bar{i}_{sq} = (0.9 \sim 0.99) \frac{3\sqrt{3}}{\pi}|E_g| i_b \quad (13)$$

From the (13), the relationship between i_b and \bar{i}_{sq} is as follows:

$$\bar{i}_{sq} = -(0.99 \sim 1.09) i_b \quad (14)$$

Figure 7(b) shows the average values of i_{sq} and boost converter current i_b under wind speed profile of Fig. 7(a) for the study 2 MW PMSG-based WT with parameters of Appendix A. Considering (14) and Fig. 7, in a wide range of wind speed variations, the average values of i_{sq} and i_b are approximately identical, i.e. $|\bar{i}_{sq}| \cong i_b$. Therefore, from (3), the PMSG torque as a function of i_b is approximately given by

$$T_e = -\frac{3}{2} \frac{p}{2} n_p (\psi_{pm} i_b) \quad (15)$$

4. Different control strategies of the study system

In this section according to main duties of the boost converter and GSC, three control strategies are briefly introduced for the study system. In the first control strategy, according to Fig. 8(a), the boost converter is responsible for the generator speed control at the MPPT mode and GSC is used for the dc-link voltage control. In the second control strategy, according to Fig. 8(b), the boost converter is used to adjust the PMSG active power at the reference value, and GSC adjusts the dc link voltage to its set point value. In the third control strategy, as clear from Fig. 8(c), the boost converter regulates the dc link voltage, and GSC adjusts the active power injected to the grid to a reference value corresponding to MPPT mode. It is noted that at all three mentioned control strategies, the study system is controlled in the MPPT mode, and the reference of the generator speed/active power is achieved according to the power-speed curve.

Detailed representations and block diagrams of these control strategies will be given in Sections 4.2, 4.3 and 4.4.

4.1 Estimation of rotor speed in PMSG-WT with boost converter and diode rectifier

In all three mentioned control strategies mentioned above the generator speed is required for the control of the study system. In this section, a method is presented for estimation of the generator speed.

According to (9), the rectifier output voltage v_d may be given as $v_d = v_{d0} - \frac{3}{\pi} X_s i_b$, where the first term $v_{d0} = (3\sqrt{3}/\pi) \omega_r \psi_{pm} = k \omega_r$, known as no load voltage, is proportional to generator speed, and the second term $\frac{3}{\pi} X_s i_b$ is the voltage drop due to commutation procedure. Table 1 depicts the values of the first and second items at different wind speeds. As stated before, and it is clear from Table 1, the contribution of the term $\frac{3}{\pi} X_s i_b$ in v_d is negligible, and we can approximately express $v_d \cong (3\sqrt{3}/\pi) \omega_r \psi_{pm}$. However, since $v_{d0} = k \omega_r$, the accurate estimation of the generator speed can be realized through measuring v_d and computing v_{d0} ($v_d = v_{d0} - \frac{3}{\pi} X_s i_b$). Figure 9 demonstrates the block diagram for accurate estimation of the generator speed, where ω_r^n and v_{d0}^n correspond to rated generator speed and power.

4.2 System control structure at the first control strategy

In this section, the control block diagrams of the boost converter and GSC with the first control strategy are presented.

4.2.1 Boost converter control with the first control strategy

According to (15), the electromagnetic torque T_e is directly related to the boost converter current i_b . Hence, the generator speed may be controlled by adjusting i_b through duty cycle of boost converter switch. Figure 10 illustrates the overall block-diagram of the boost converter control with the first control strategy. The control structure of the boost converter includes the outer generator speed and

inner current control loops, where the boost converter reference current is obtained from the outer control loop of the generator speed.

Figure 11 demonstrates the generator speed control loop, in which $\alpha_b/(s + \alpha_b)$ denotes the transfer function of the boost converter current control loop.

Since the outer speed control loop is much slower than the inner current control loop, in the speed control loop, it is possible to ignore the inner current control dynamics and thus replaces $\alpha_b/(s + \alpha_b)$ with 1. Therefore, the closed-loop transfer function of the generator speed control is achieved as given below.

$$\frac{\omega_r}{\omega_{r-ref}} = \frac{(3n_p \psi_{pm}/4H_g)(k_{p\omega}s + k_{i\omega})}{s^2 + (3n_p \psi_{pm} k_{p\omega}/4H_g)s + (3n_p \psi_{pm} k_{i\omega}/4H_g)} \quad (16)$$

According to (16), we obtain the parameters of PI controller, $k_{p\omega}$ and $k_{i\omega}$, from the following equation:

$$\begin{aligned} 2\xi\omega_n &= (3n_p \psi_{pm} k_{p\omega}/4H_g) \\ \omega_n^2 &= (3n_p \psi_{pm} k_{i\omega}/4H_g) \end{aligned} \quad (17)$$

where ω_n and ξ correspond to the undamped natural frequency and damping ratio of the control loop, respectively. Due to direct relation between the ω_n and closed loop bandwidth of the outer control loop, ω_n is selected much smaller than the bandwidth of the inner current control loop (α_b), because the dynamics of the outer speed control loop is much slower than the dynamics of the current control loop. Hence, the PI controller parameters of the generator speed control, i.e. $k_{p\omega}$ and $k_{i\omega}$, are obtained from (17) by setting $\omega_n = 2\pi \times 1$ rad/s and $\xi = 0.7$.

In Fig. 11, the reference speed ω_r^* is selected such that the WT works in the MPPT mode at the rotational speeds below the rated one. At high wind speeds, the MPPT mode is not realized and generator speed is set to its rated one. The stator output active power at the MPPT mode may be considered as $P_s = k_{opt} \omega_r^3$.

4.2.2 GSC control with the first control strategy

In the first control strategy, the GSC can set the dc-link voltage at the reference value. As stated before, the GSC is controlled in the dq frame with GVO, and thus in Fig. 1, the active power injected

to the grid can be given as $P_g = v_{gd} i_{gd}$. From Fig. 1 and by ignoring the converters losses, the dc-link power balance equation is expressed as

$$(P_b - P_g) = C_{dc} v_{dc} \frac{dv_{dc}}{dt} \quad (18)$$

where P_b is the boost converter input active power, v_{dc} and C_{dc} are the dc-link voltage (in volt) and capacitor (in F). Linearizing (18) around the operating point results in the following equation:

$$(\Delta P_b - \Delta P_g) = C_{dc} v_{dc0} \frac{d\Delta v_{dc}}{dt} \quad (19)$$

where Δ depicts the small-signal deviation about the operating point. Figure 12 illustrates the closed-loop control of the dc-link voltage. The term $\alpha_g / (s + \alpha_g)$ in Fig. 12 corresponds to the closed-loop transfer function of the inner current control loop. If the dc-link dynamics is slow enough compared to the inner current control loop, we can set i_{gd} to its set point value i_{gd}^* , and thus for the frequency range of $\omega \ll \alpha_g$, the dynamics of $\alpha_g / (s + \alpha_g)$ in Fig. 12 can be ignored. Therefore, the transfer function from v_{dc}^* to v_{dc} may be described by

$$\frac{v_{dc}}{v_{dc}^*} = \frac{2\xi\omega_n s + \omega_n^2}{s^2 + 2\xi\omega_n s + \omega_n^2} \quad (20)$$

where ω_n and ξ correspond to the closed-loop bandwidth and the damping ratio of the dc-link voltage control loop, respectively and $\omega_n^2 = 3|V_g|k_{i_{-dc}} / 2C_{dc}V_{dc0}$, $2\xi\omega_n = 3|V_g|k_{p_{-dc}} / 2C_{dc}V_{dc0}$.

In the grid voltage oriented reference frame, i_{gd} can be used for the dc-link voltage control and i_{gq} for the reactive power control. Usually i_{gq}^* is considered equal to zero and thus the GSC works at unity power factor. Figure 13 demonstrates the overall control structure of the GSC in the first control strategy.

4.3 System control structure at the second control strategy

In the second control strategy, the boost converter is responsible for the control of the PMSG output active power. Considering (8) and Fig. 5 and under disregarding the stator resistance, the PMSG active power may be given by

$$P_s = -\frac{3}{2} \omega_r \psi_{pm} i_{sq} \quad (21)$$

As shown in Section 3, $i_{sq} = -i_b$, and thus the PMSG active power in terms of the boost converter current may be given as

$$P_s \cong \frac{3}{2} \omega_r \psi_{pm} i_b \quad (22)$$

The linearized form of (22) about the operating point can be given as

$$\Delta P_s = \left(\frac{3}{2} \omega_{r0} \psi_{pm} \right) \Delta i_b + \left(\frac{3}{2} \psi_{pm} i_{b0} \right) \Delta \omega_r \quad (23)$$

Figure 14 demonstrates the overall control block diagram of the boost converter in the second control strategy. The boost converter control structure includes the outer and inner control loops of the PMSG active power and boost converter current, respectively.

From (23), the PMSG active power control loop is achieved as given in Fig. 15. In Fig. 15, $\alpha_b / (s + \alpha_b)$ is the current control loop transfer function of the boost converter.

From Fig. 15, the closed-loop transfer function of the PMSG active power control is attained as given below.

$$\frac{P_s}{P_s^*} = \frac{\left(\frac{3}{2} k_{pP} \omega_{r0} \psi_{pm} \alpha_b \right) s + \left(\frac{3}{2} k_{iP} \omega_{r0} \psi_{pm} \alpha_b \right)}{s^2 + \alpha_b \left(1 + \frac{3}{2} k_{pP} \omega_{r0} \psi_{pm} \right) s + \left(\frac{3}{2} k_{iP} \omega_{r0} \psi_{pm} \alpha_b \right)} \quad (24)$$

According to (24), the PI controller parameters k_{pP} and k_{iP} are obtained from the following equation:

$$\begin{aligned} 2\xi\omega_n &= \alpha_b \left(1 + \frac{3}{2} k_{pP} \omega_{r0} \psi_{pm} \right) \\ \omega_n^2 &= \left(\frac{3}{2} k_{iP} \omega_{r0} \psi_{pm} \alpha_b \right) \end{aligned} \quad (25)$$

where ω_n and ξ correspond to the undamped natural frequency and damping ratio of the PMSG active power control loop, respectively. Since the outer control loop should be much slower than the inner control loop, by selecting $\omega_n = 0.1\alpha_b$ and $\xi = 0.7$, the controller parameters are achieved. In Fig. 15, the reference power P_s^* is selected such that the WT operates in the MPPT mode at the rotational speeds below the rated one. At high wind speeds, the WT cannot operate in the MPPT mode and PMSG active power is set to its rated value. As stated before, the stator output active power at the MPPT mode can be approximated as $P_s = k_{opt} \omega_r^3$.

The main function of the GSC in the second control strategy is keeping the dc-link voltage constant and regulation of the reactive power delivered to the grid. Hence, the control structures of the GSC in the first and second control strategies are exactly similar, and thus, are not given in this section.

4.4 System control structure at the third control strategy

In the following, the control block diagrams of the boost converter and GSC at the third control strategy are presented.

4.4.1 Boost converter control at the third control strategy

In the third control strategy, the boost converter regulates the dc-link voltage to the set point value. According to Fig. 2, the dc-link voltage dynamics can be described by

$$(1-d)i_b - i_{dc} = C_{dc} \frac{dv_{dc}}{dt} \quad (26)$$

The linearized form of (26) about the operating point can be given as

$$(1-d_0)\Delta i_b - \Delta d \cdot i_{b0} - \Delta i_{dc} = C_{dc} \frac{d\Delta v_{dc}}{dt} \quad (27)$$

Figure 16 demonstrates the overall boost converter control in the third control strategy. The boost converter control structure includes the outer and inner control loops of the dc link voltage and boost converter current, respectively.

From (27), the dc-link voltage control loop by the boost converter is attained as given in Fig. 17. In Fig. 17, $\alpha_b/(s + \alpha_b)$ represents the transfer function related to boost converter current control loop.

If dynamics of the dc-link is slow enough compared to the inner current control loop, we can set i_b equal to set point value i_b^* , and therefore for the frequency range $\omega \ll \alpha_b$, the dynamics of $\alpha_b/(s + \alpha_b)$ in

Fig. 17 can be ignored. Therefore, the transfer function from v_{dc}^* to v_{dc} may be given as:

$$\frac{v_{dc}}{v_{dc}^*} = \frac{2\xi\omega_n s + \omega_n^2}{s^2 + 2\xi\omega_n s + \omega_n^2} \quad (20)$$

where ω_n and ξ correspond to the bandwidth and damping ratio of the dc-link voltage control loop, respectively and $\omega_n^2 = k_i(1-d_0)/C_{dc}$, $2\xi\omega_n = k_p(1-d_0)/C_{dc}$.

4.4.2 GSC control structure with the third control strategy

In the third control mode, the GSC sets the grid injected active and reactive powers to their reference values. As stated before, in the grid voltage oriented reference frame, i_{gd} and i_{gq} are used for the active and reactive power regulation, respectively. Figure 18 demonstrates the control loop of the GSC active power.

P_g^* in Fig. 18 is the GSC active power reference and is selected for operation of the WT in the MPPT mode. For operation in the MPPT mode and under neglecting the converter losses, P_g^* may be considered as $k_{opt} \omega_r^3$ for the generator speed blow the rated one. Figure 19 illustrates the overall block diagram of the GSC control system in the third control mode, where i_{gd} controls P_g and i_{gq} is adjusted to zero for operation at unity power factor.

5. Simulation results

Performance of the PMSG-WT in the study system of Fig. 1 is examined in this section, and capabilities of the three control strategies presented in Section 4 are investigated and compared. The study system in Fig. 1 includes a 2 MW--690 V--50 Hz PMSG-based WT with parameters of Appendix A that is linked to a 20 kV grid through a 690 V/20 KV transformer and transmission line.

Figure 20 demonstrates the wind speed profile and corresponding generator speed response. Figure 20(b) indeed depicts the estimated and actual values of the generator speed, and based on which, it is clear that the estimated values of the generator speed at different wind speed are well close to the actual ones.

Figure 21 shows steady state responses of the PMSG-based WT for the three mentioned control strategies mentioned in Section 4 and against wind speed change from 10 to 12 m/s. Figure 21 indeed illustrates responses of the generator speed, stator active power, dc-link voltage and electromagnetic torque. From Fig. 21, it is evident that WT responses are relatively identical for all three control strategies mentioned in Section 4.

Figure 22 shows the three-phase and dq parts of the stator current and boost converter current for the wind speed of 12 m/sec. In Fig. 22, because of existence of the diode-rectifier, the three-phase stator currents contain the fundamental and harmonic frequencies. Therefore, as shown in Fig. 22(a) and (b), i_{sd} and i_{sq} are not constant and include ac harmonic ripples. In Fig. 22, the mean values of i_{sq} and boost

converter current i_b are approximately identical and equal to 2590 A, and this is in close agreement with the result of Section 3.

Figure 23 describes responses of the dc-link voltage, stator active power, generator torque and boost converter current against 70% three-phase voltage dip at $t=4$ sec, for the three mentioned control strategies. Also, Fig. 24 shows the WT time responses under 90% three-phase voltage dip, for all three mentioned control strategies.

As stated before, in the first control strategy, the boost converter is responsible for the generator speed control and GSC adjusts the dc-link voltage at its reference value. In the second control strategy, the boost converter sets the PMSG active power at the reference value, and GSC adjusts the dc-link voltage to its set point value. In the third control strategy, the boost converter adjusts the dc link voltage at the reference value, and GSC controls the injected active power to the grid to a reference value corresponding to the MPPT mode.

According to Fig. 23(a) and under 70% voltage dip, the peak values of the dc-link voltage during the fault for the first, second and third control strategies are 1550 v, 2000 v and 1350 v, respectively. Also, according to Fig. 24(a) and under 90% voltage dip, the peak values of the dc-link voltage for the first, second and third control strategies are 2000 v, 2420 v and 1400 v, respectively.

According to Figs. 23(a) and 24(a), it is clear that the peak values of the dc-link voltage during the fault for the third control strategy are lower than the ones in the first and second control strategies. Hence, the LVRT capability of the wind-turbine enhances significantly in the third control structure without any hardware protection. Since, in the third control structure, MSC is responsible for the dc-link voltage control via q-axis stator current, the stator output active power, generator torque and boost converter current decrease during the voltage dip in this control structure (see Figs. 23(b), (c) and (d) and Figs. 24(b), (c) and (d)). Hence, according to Figs. 23(b) and 24(b), in the third control structure, the power exported from the stator to the dc-link decreases during the voltage dip, and this lessens the dc-link overvoltage in the third control structure during fault conditions.

6. Conclusion

In this paper, performance analysis and control of the PMSG-WT, implementing boost converter and diode-rectifier as the machine-side converter, is presented. In the paper, at first, the relation between the active component of the stator current and boost converter current is extracted, a simple and

efficient approach is presented for the generator speed estimation, and then, three sensorless control strategies are presented for the control of the grid-connected PMSG-based wind turbine (WT).

At the end, features of the abovementioned three control strategies are investigated and compared against wind speed variation and grid voltage dip. In this way, steady-state and transient responses of the WT system are investigated for each mentioned control strategy in the Matlab-Simulink environment. It is shown that steady-state responses of the WT are relatively identical for all three control strategies. However, at the fault conditions, the third control strategy has better performance, and thus, the WT low-voltage ride-through behavior enhances significantly in the third control structure without any hardware protection. This is because in the third control structure, the boost converter is responsible for the dc-link voltage control, and thus, the stator output active power, generator torque and boost converter current decrease during the voltage dip in this control structure. Therefore, the power exported from the PMSG stator to the dc-link decreases during the voltage dip, and this lessens the dc-link overvoltage, in the third control structure, during the grid fault conditions.

Appendix

Parameters of the 2 MW, 690 V, 50 Hz, PMSG-WT are given below in Table 2.

References

- [1] Uehara, A., Pratap, A., Goya, T., *et al.*, “A coordinated control method to smooth wind power fluctuations of a PMSG-based WECS”, *IEEE Transactions on Energy Conversion*, 26(2), pp. 550–558 (2011).
- [2] Kasem Alaboudy, A. H., Daoud, A. A., Desouky, S. S., *et al.*, “Converter controls and flicker study of PMSG-based grid connected wind turbines”, *Ain Shams Engineering Journal*, 4(1), pp. 75–91 (2013).
- [3] Rajaei, A. H., Mohamadian, M., Dehghan, S. M., *et al.*, “PMSG-based variable speed wind energy conversion system using Vienna rectifier”, *European Transactions on Electrical Power*, 21(1), pp. 954–972 (2011).
- [4] Freire, N. M. A. and Cardoso, A. J. M., “Fault-tolerant PMSG drive with reduced DC-link ratings for wind turbine applications”, *IEEE Journal of Emerging and Selected Topics in Power Electronics*, 2(1), pp. 26–34 (2014).
- [5] Zhang, S., Tseng, K.J., Vilathgamuwa, D. M., *et al.*, “Design of a robust grid interface system for PMSG-based wind turbine generators”, *IEEE Transactions on Industrial Electronics*, 58(1), pp. 316–328 (2011).

- [6] M. Rahimi, “Mathematical modeling, dynamic response analysis and control of PMSG based wind turbines operating with an alternative control structure in power control mode”, *International Transactions on Electrical Energy Systems*, 27(12), pp. 1–18 (2017).
- [7] M. Rahimi, A. Beiki, “Efficient modification of the control system in PMSG based wind turbine for improvement of the wind turbine dynamic response and suppression of torsional oscillations”, *International Transactions on Electrical Energy Systems*, 28(8), pp. 1–16 (2018).
- [8] M. Rahimi, “Modeling, control and stability analysis of grid connected PMSG based wind turbine assisted with diode rectifier and boost converter”, *International Journal of Electrical Power & Energy Systems*, 93, pp. 84–96 (2017).
- [9] Xie, D., Lu, Y., Sun, J., et al., “Small signal stability analysis for different types of PMSGs connected to the grid”, *Renewable Energy*, 106, pp. 149–164 (2017).
- [10] Noori Khezrabad, A. and Rahimi, M., “Performance and dynamic response enhancement of PMSG based wind turbines employing boost converter-diode rectifier as the machine-side converter”, *Scientia Iranica*, Articles in Pres, (2020).
- [11] Urtasun, A., Sanchis, P., San Martín, I., et al., “Modeling of small wind turbines based on PMSG with diode bridge for sensorless maximum power tracking”, *Renewable Energy*, 55, pp. 138–149 (2013).
- [12] Aubrée, R., Auger, F., Macé, M., et al., “Design of an efficient small wind-energy conversion system with an adaptive sensorless MPPT strategy”, *Renewable Energy*, 86, pp. 280–291 (2016).
- [13] Șerban, I. and Marinescu, C., “A sensorless control method for variable-speed small wind turbines”, *Renewable Energy*, 43, pp. 256–266 (2012).
- [14] Yu, K. N. and Liao, C. K., “Applying novel fractional order incremental conductance algorithm to design and study the maximum power tracking of small wind power systems”, *Journal of Applied*
- [15] Mozayan, S. M., Saad, M., Vahedi, H., et al., “Sliding mode control of PMSG wind turbine based on enhanced exponential reaching law”, *IEEE Transactions on Industrial Electronics*, 63(10), pp. 6148–6159 (2016).
- [16] Dursun, E. H. and Kulaksiz, A. A., “Second-order sliding mode voltage-regulator for improving MPPT efficiency of PMSG-based WECS”, *International Journal of Electrical Power & Energy Systems*, 121, p. 106149 (2020).
- [17] Liang, C., Le Claire, J.-C., Aït-Ahmed, M., et al., “Power control of 5-phase PMSG-diode rectifier-interleaved boost set under health and fault modes”, *Electric Power Systems Research*, 152, pp. 316–322 (2017).
- [18] Yaramasu, V., Wu, B., Alepuz, S., et al., “Predictive control for low-voltage ride-through enhancement of three-level-boost and NPC-converter-based PMSG wind turbine”, *IEEE Transactions on Industrial Electronics*, 61(12), pp. 6832–6843 (2014).

- [19] Yaramasu, V. and Wu, B., “Predictive control of a three-level boost converter and NPC inverter for high-power PMSG-based medium voltage wind energy conversion systems”, *IEEE Transactions on Power Electronics*, 29(10), pp. 5308–5322 (2014).
- [20] Milev, K., Yaramasu, V., Dekka, A., et al., “Predictive control of multichannel boost converter and VSI-based six-phase PMSG wind energy systems with fixed switching frequency”, *11th Power Electronics, Drive Systems, and Technologies Conference (PEDSTC)*, pp. 1–6 (2020).
- [21] Milev, K., Alshammari, F., Yaramasu, V., et al., “Predictive control with fixed switching frequency for three-level boost and NPC converters interfaced PMSG wind turbine”, *3rd International Conference on Energy, Power and Environment: Towards Clean Energy Technologies*, pp. 1–6 (2021).
- [22] Barote, L., Marinescu, C., and Cirstea, M. N., “Control structure for single-phase stand-alone wind-based energy sources”, *IEEE Transactions on Industrial Electronics*, 60(2), pp. 764–772 (2013).
- [23] Mesbahi, A., Saad, A., Khafallah, M., et al., “Boost converter analysis to optimize variable speed PMSG wind generation system”, *International Renewable and Sustainable Energy Conference (IRSEC)*, pp. 275–280 (2013).
- [24] Putri, R. I., Pujiantara, M., Priyadi, A., et al., “Maximum power extraction improvement using sensorless controller based on adaptive perturb and observe algorithm for PMSG wind turbine application”, *IET Electric Power Applications*, 12(4), pp. 455–462 (2018).
- [25] Alsokhiry, F., Abdelsalam, I., Adam, G. P., et al., “High-power medium-voltage three-phase ac–dc buck–boost converter for wind energy conversion systems”, *Electric Power Systems Research*, 177, p. 106012 (2019).
- [26] Chinchilla, M., Arnaltes, S., and Burgos, J. C., “Control of permanent-magnet generators applied to variable-speed wind-energy systems connected to the grid”, *IEEE Transactions on Energy Conversion*, 21(1), pp. 130–135 (2006).
- [27] Tripathi, S. M., Tiwari, A. N., and Singh, D., “Optimum design of proportional-integral controllers in grid-integrated PMSG-based wind energy conversion system”, *International Transactions on Electrical Energy Systems*, 26(5), pp. 1006–1031 (2016).
- [28] Zhang, X., Wu, Z., Hu, M., et al., “Coordinated control strategies of VSC-HVDC-based wind power systems for low voltage ride through”, *Energies*, 8(7), pp. 7224–7242 (2015).
- [29] Dang, C.-L., Zhang, L., and Zhou, M.-X., “Optimal power control model of direct driven PMSG”, *Energy Procedia*, 12, pp. 844–848 (2011).
- [30] Alizadeh, O. and Yazdani, A., “A control strategy for power regulation in a direct-drive WECS with flexible drive-train”, *IEEE Transactions on Sustainable Energy*, 5(4), pp. 1156–1165 (2014).
- [31] Hansen, A. D. and Michalke, G., “Modelling and control of variable-speed multi-pole permanent magnet synchronous generator wind turbine”, *Wind Energy*, 11(5), pp. 537–554 (2008).

- [32] Yuan, X., Wang, F., Boroyevich, D., et al., “DC-link voltage control of power converter for wind generator operating in weak-grid systems”, *IEEE Transactions on Power Electronics*, 24(9), pp. 2178–2192 (2009).
- [33] Hansen, A. D. and Michalke, G., “Multi-pole permanent magnet synchronous generator wind turbines’ grid support capability in uninterrupted operation during grid faults”, *IET Renewable Power Generation*, 3(3), pp. 333–348 (2009).
- [34] Van, T. L., Ngyen, T. D., Tran, T. T., et al., “Advanced control strategy of back-to-back PWM converters in PMSG wind power system”, *Advances in Electrical and Electronic Engineering*, 13(2), pp. 81–95 (2015).
- [35] Nguyen, P. T. H., Stüdli, S., Braslavsky, J. H., et al., “Coordinated control for low voltage ride through in PMSG wind turbines”, *IFAC-PapersOnLine*, 51(28), pp. 672–677 (2018).
- [36] Mohan N., Undeland T. M., Robbins W. P., “Power electronics: converters, applications, and design”, 3rd edition, Wiley, (2002).

Figure captions:

Fig. 1 Overall structure of the system under study

Fig. 2 Average model of the boost converter over one switching cycle

Fig. 3 Boost converter current control loop

Fig. 4 Current control loops of the GSC in the dq reference frame

Fig. 5 One-phase equivalent circuit of the PMSG

Fig. 6 PMSG and boost converter equivalent circuit at steady state conditions

Fig. 7 (a) Wind speed profile, (b) comparison of average values of the boost converter current and stator q-axis current under wind speed profile of Fig. 7(a)

Fig. 8 Overall control structures of the study system related to three different control strategies, (a) first control strategy, (b) second control strategy, (c) third control strategy

Fig. 9 Estimation of the generator speed

Fig. 10 Overall block diagram of the boost converter control

Fig. 11 Outer speed control loop at the first control strategy

Fig. 12 Closed loop control of the dc-link voltage with the first control strategy

Fig. 13 Overall control structure of the GSC in the first control strategy

Fig. 14 Overall control block diagram of the boost converter in the second control strategy

Fig. 15 Outer PMSG active power control loop with the second control strategy

Fig. 16 Overall control of the boost converter in the third control strategy

Fig. 17 Outer control loop related to dc-link voltage with the third control strategy

Fig. 18 Control loop of the GSC active power

Fig. 19 Overall control structure of the GSC in the third control strategy

Fig. 20 (a) wind speed profile, (b) actual and estimated responses of the generator speed against wind speed profile of Fig. 20(a)

Fig. 21 System time responses with the mentioned three control strategies and against the wind speed change from 10 to 12 m/s, (a) generator speed, (b) stator active power, (c) electromagnetic torque, (d) dc-link voltage

Fig. 22 Time responses of the PMSG-based WT at wind speed of 12 m/s, (a) three-phase stator current, (b) d-axis stator current, (c) q-axis stator current, (d) boost converter current

Fig. 23 System time responses with the mentioned three control strategies against 70% grid voltage dip at $t=4$ s, (a) dc-link voltage, (b) stator active power, (c) electromagnetic torque, (d) boost converter current

Fig. 24 System time responses with the mentioned three control strategies against 90% grid voltage dip at $t=4$ s, (a) dc-link voltage, (b) stator active power, (c) electromagnetic torque, (d) boost converter current

Table captions:

Table 1 Contributions of the first and second items on the average output voltage of the rectifier

Table 2 System under study parameters

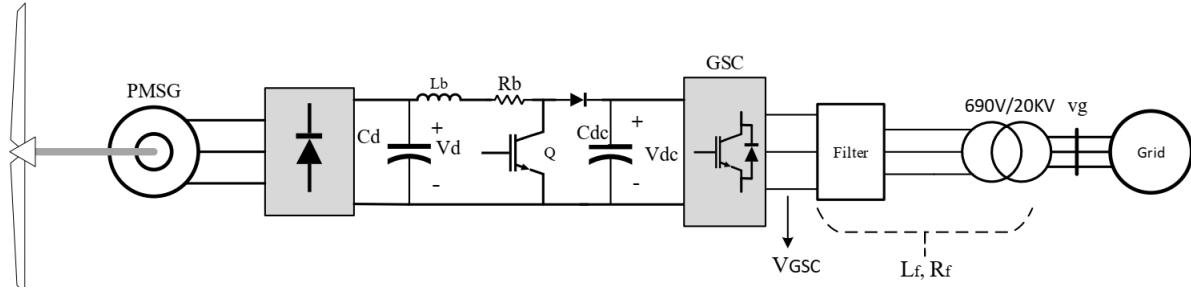


Fig. 1 Overall structure of the system under study

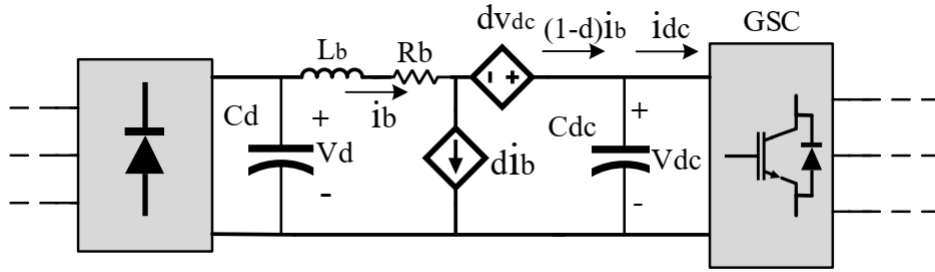


Fig. 2 Average model of the boost converter over one switching cycle

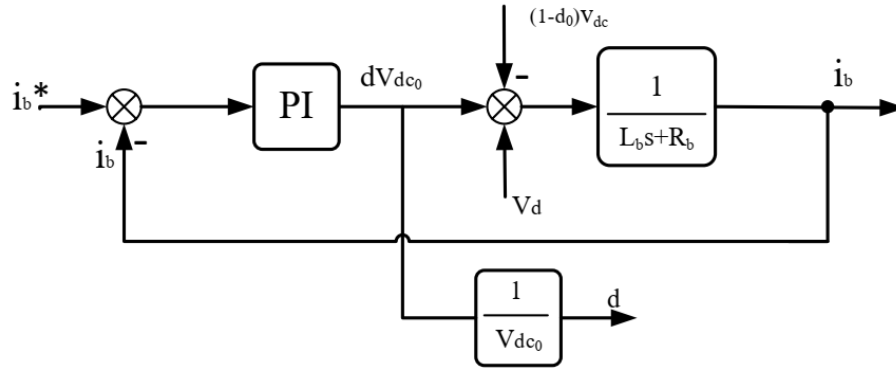


Fig. 3 Boost converter current control loop

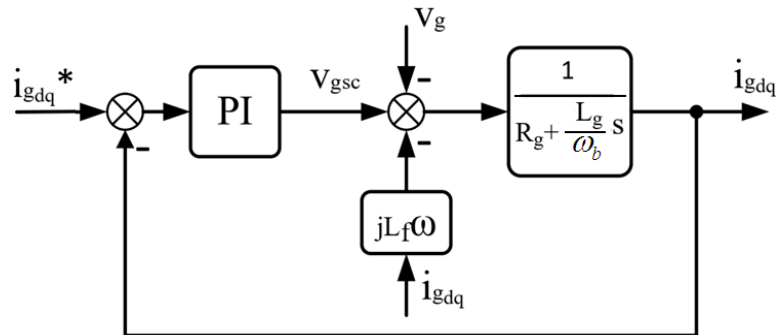


Fig. 4 Current control loops of the GSC in the dq reference frame

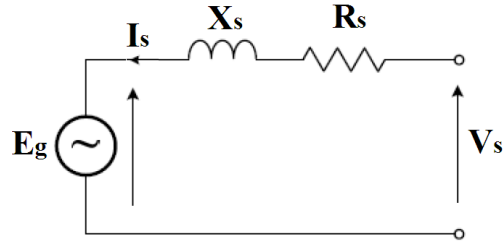


Fig. 5 One-phase equivalent circuit of the PMSG

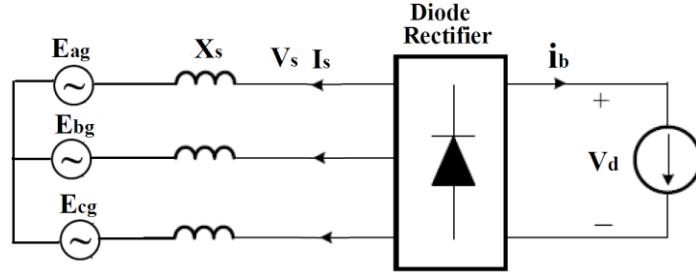


Fig. 6 PMSG and boost converter equivalent circuit at steady state conditions

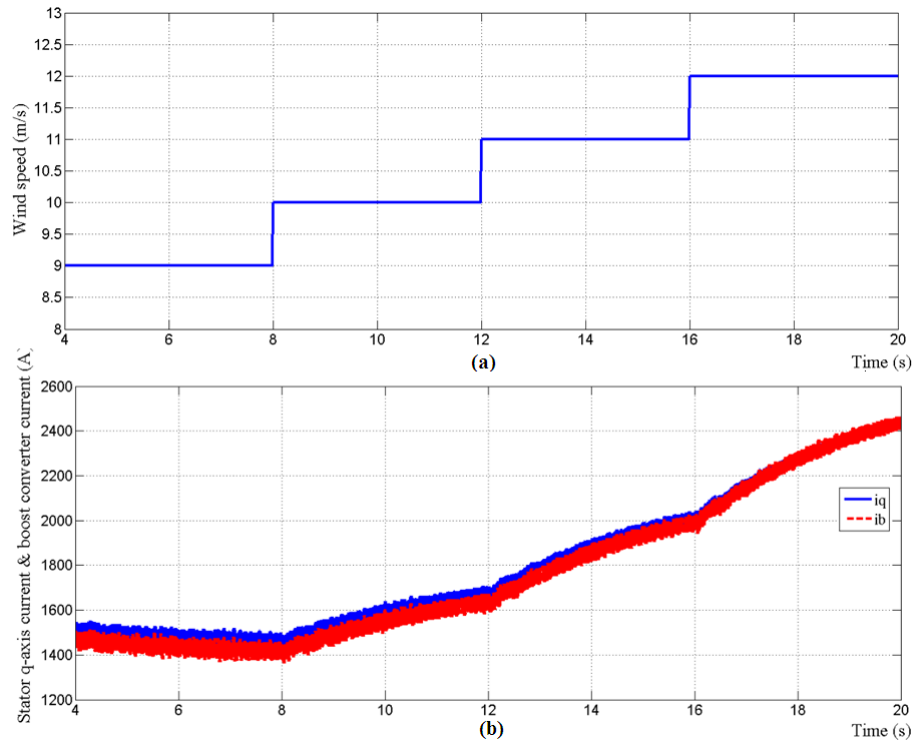
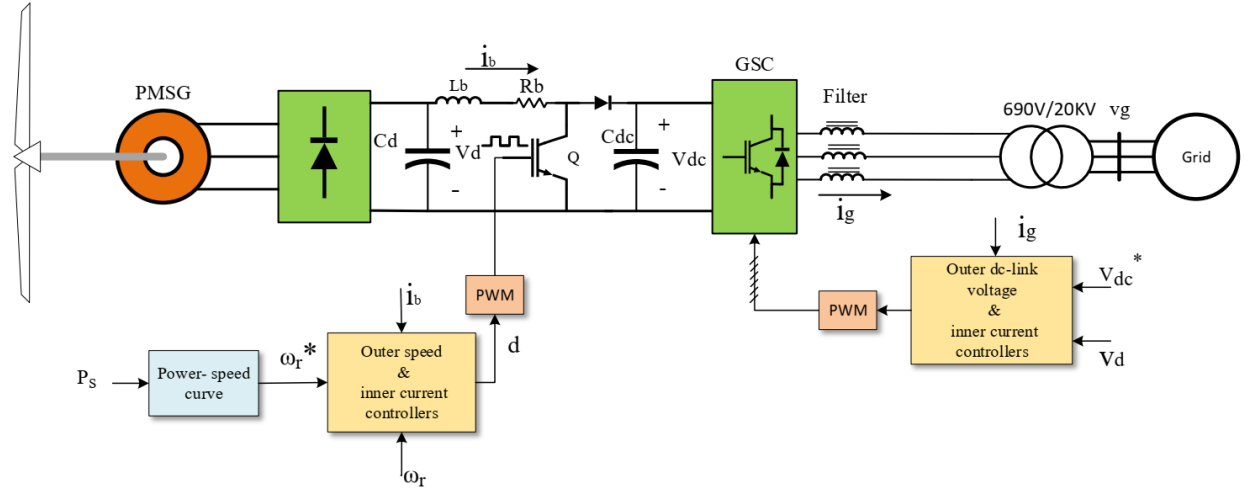
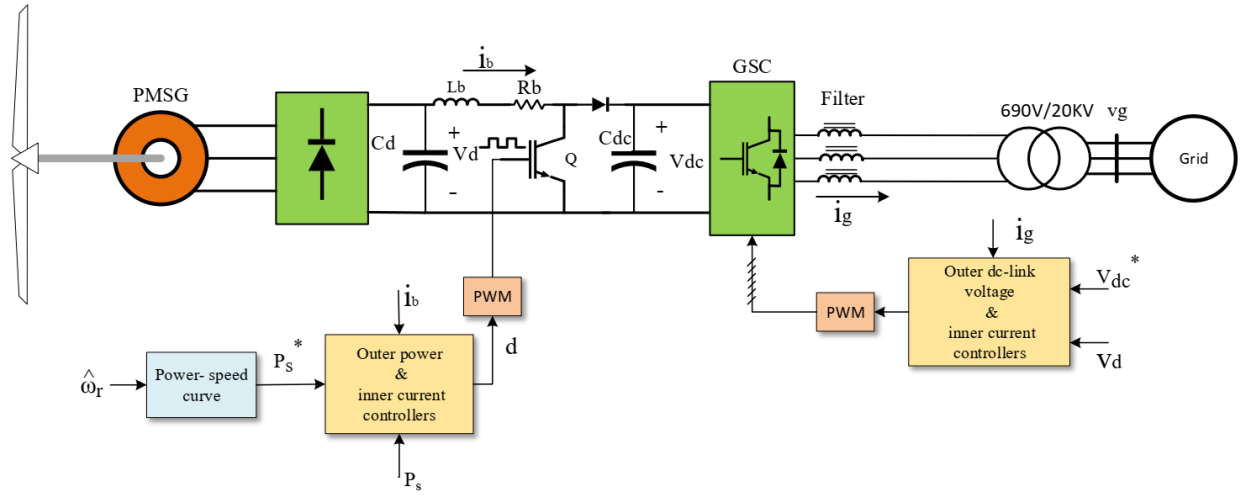


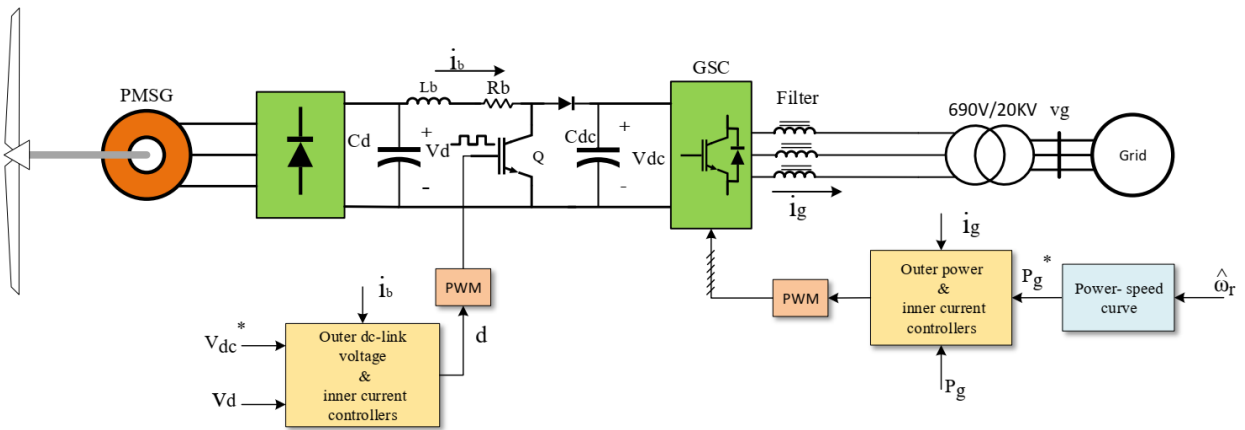
Fig. 7 (a) Wind speed profile, (b) comparison of average values of the boost converter current and stator q-axis current under wind speed profile of Fig. 7(a)



(a)



(b)



(c)

Fig. 8 Overall control structures of the study system related to three different control strategies, (a) first control strategy, (b) second control strategy, (c) third control strategy

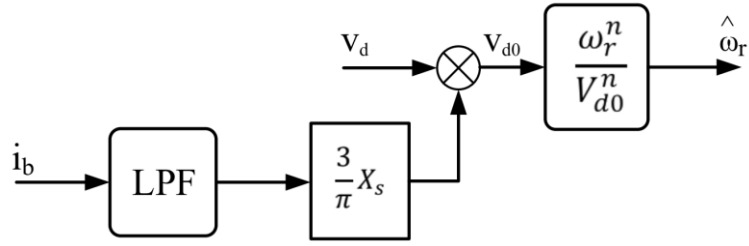


Fig. 9 Estimation of the generator speed

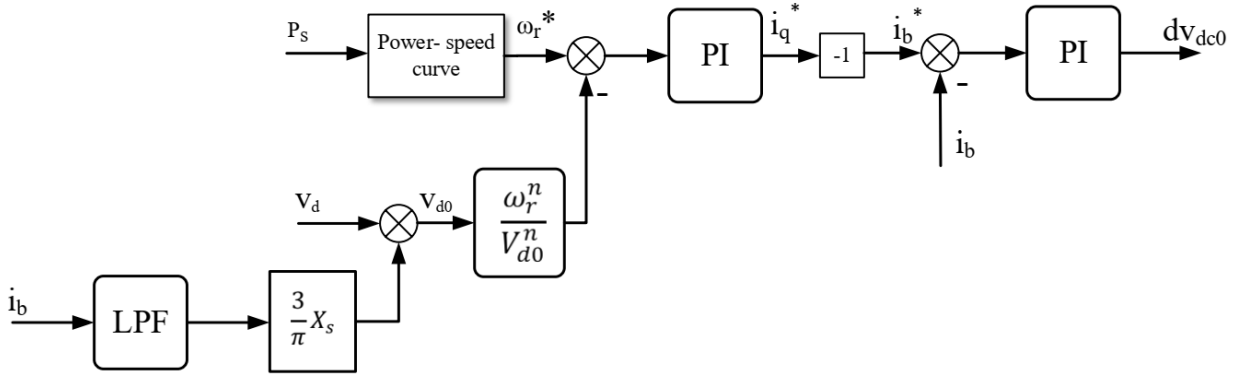


Fig. 10 Overall block diagram of the boost converter control

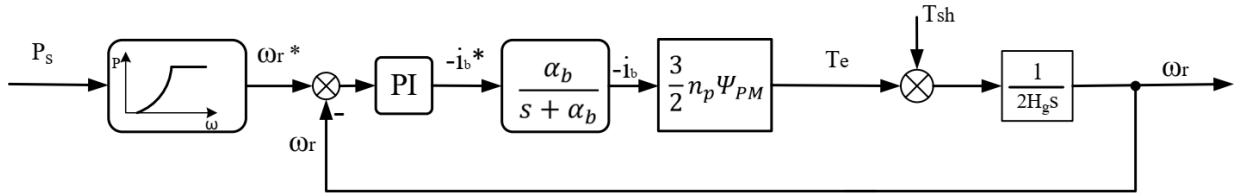


Fig. 11 Outer speed control loop at the first control strategy

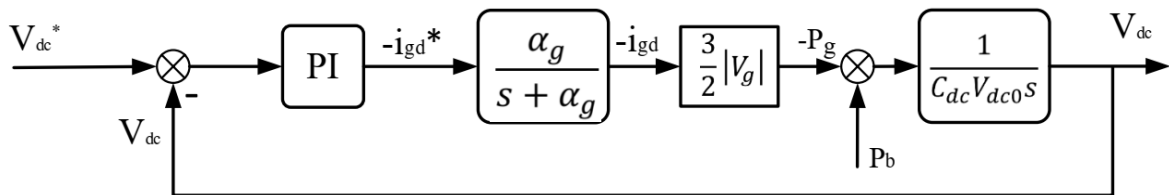


Fig. 12 Closed loop control of the dc-link voltage with the first control strategy

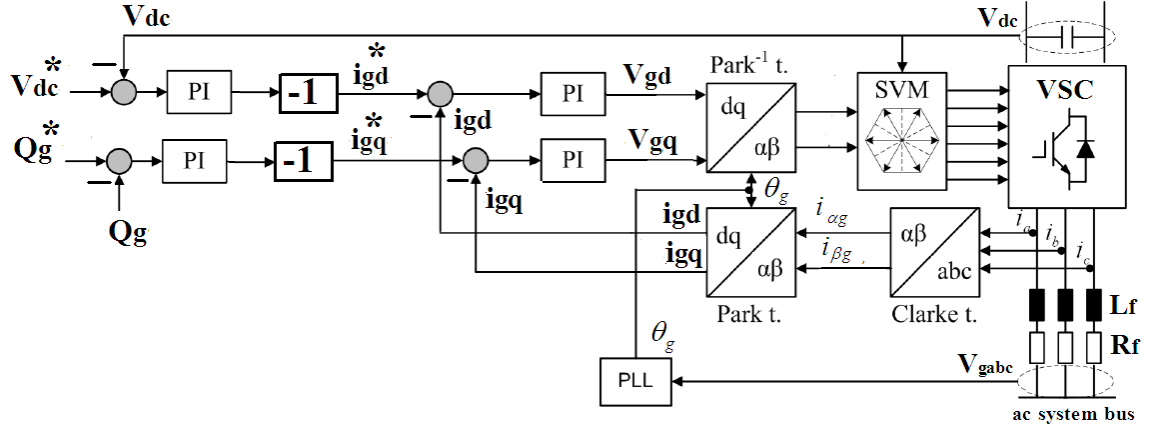


Fig. 13 Overall control structure of the GSC in the first control strategy

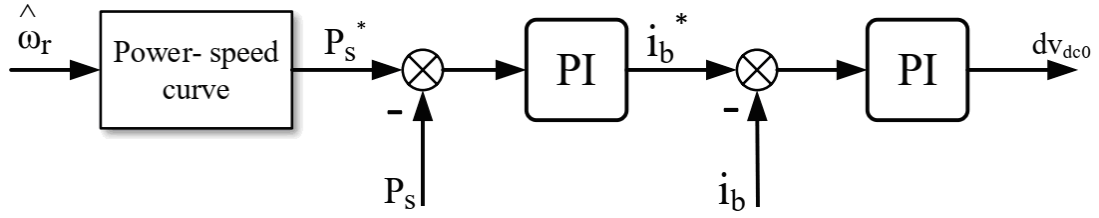


Fig. 14 Overall control block diagram of the boost converter in the second control strategy

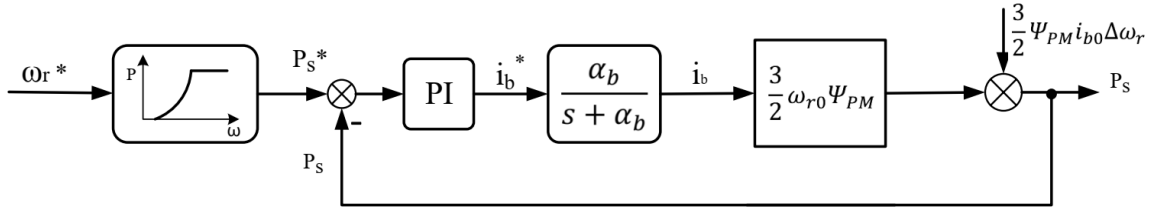


Fig. 15 Outer PMSG active power control loop with the second control strategy

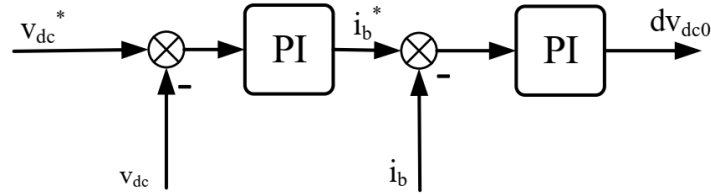


Fig. 16 Overall control of the boost converter in the third control strategy

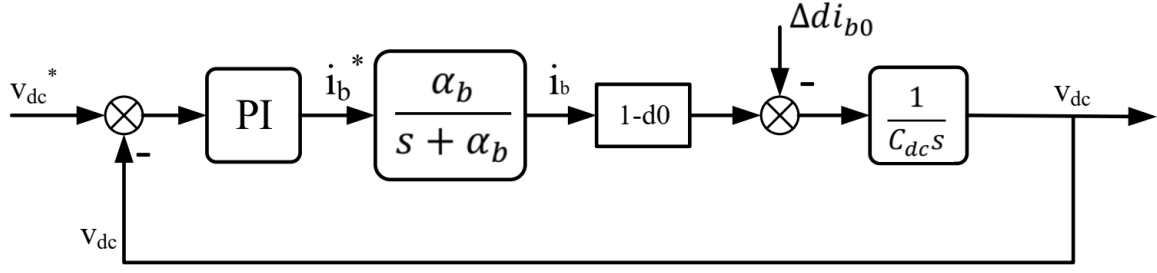


Fig. 17 Outer control loop related to dc-link voltage with the third control strategy

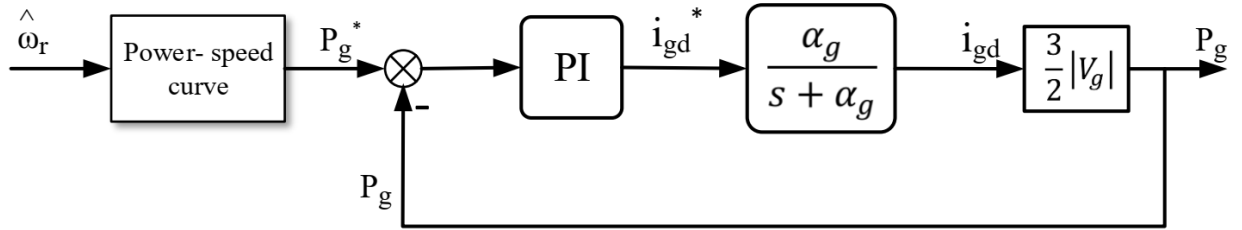


Fig. 18 Control loop of the GSC active power

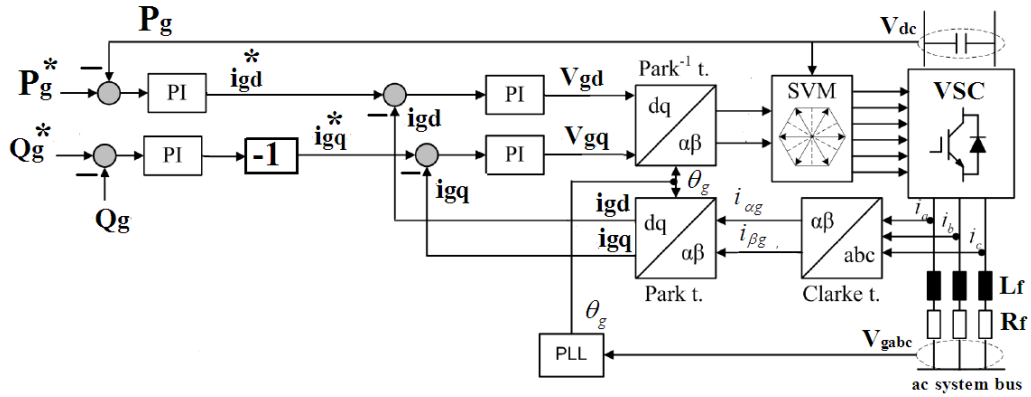
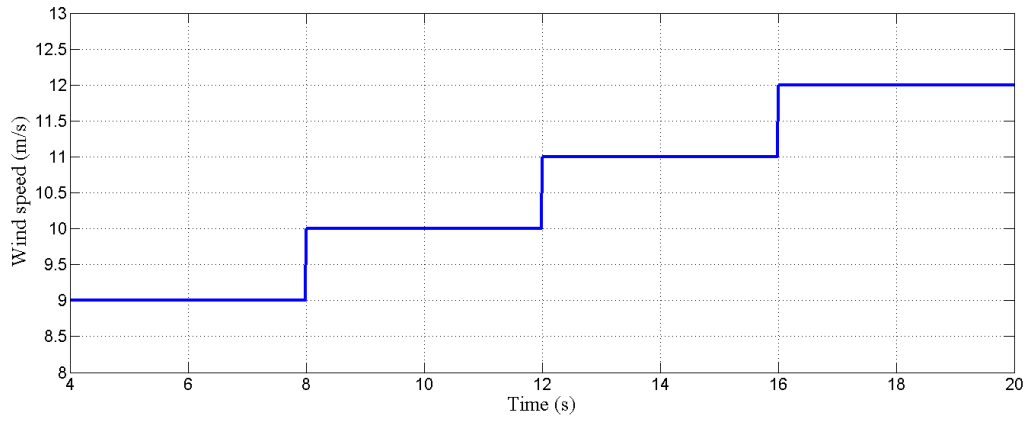
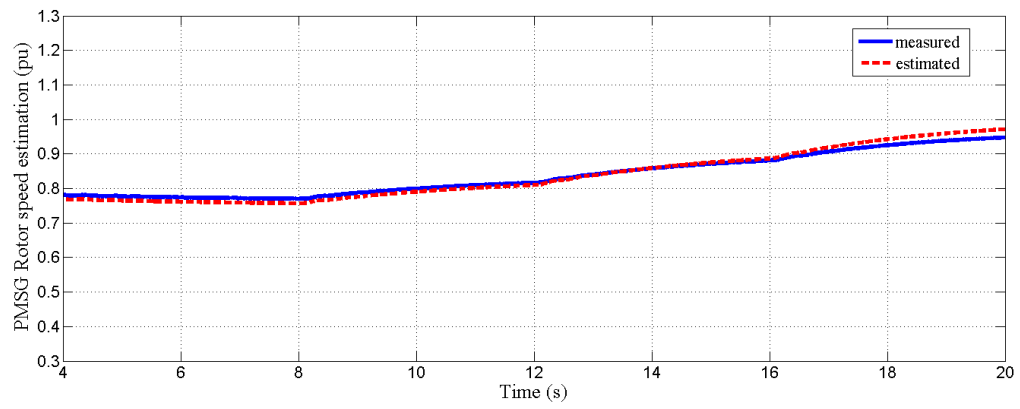


Fig. 19 Overall control structure of the GSC in the third control strategy



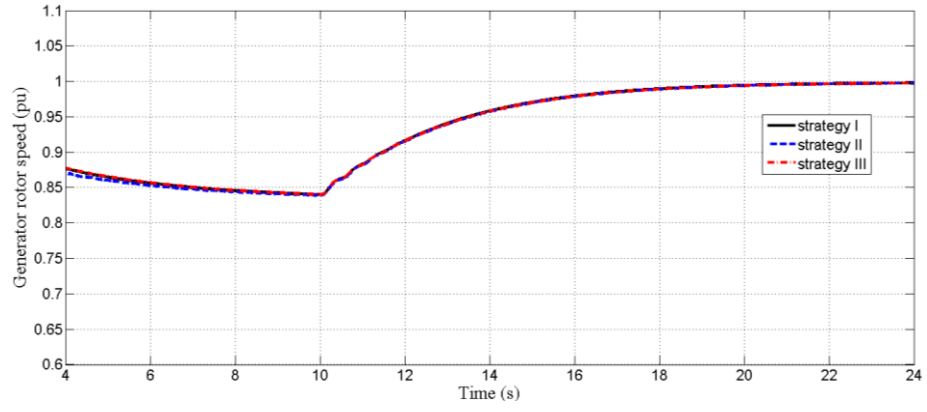
(a)



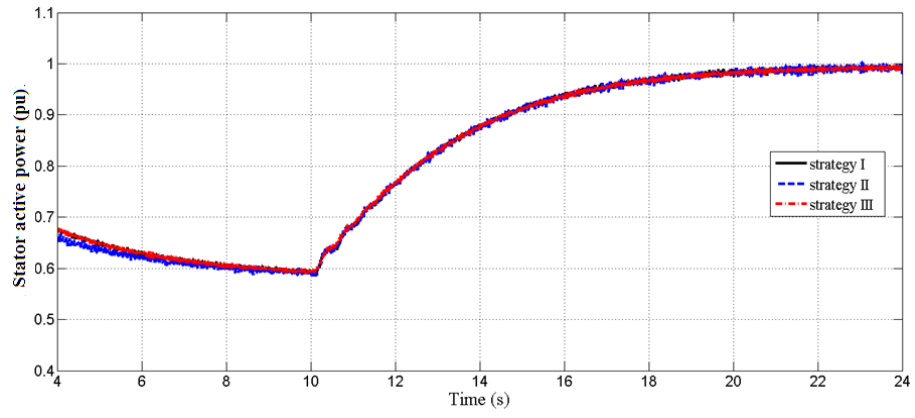
(b)

Fig. 20 (a) wind speed profile, (b) actual and estimated responses of the generator speed against wind speed profile of Fig.

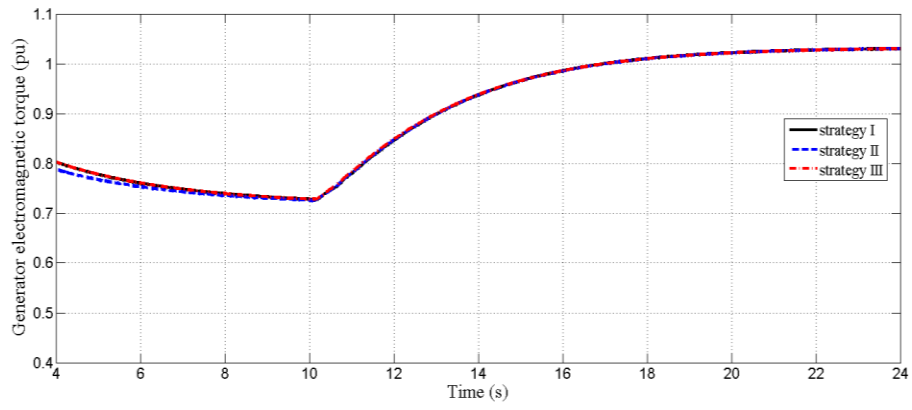
20(a)



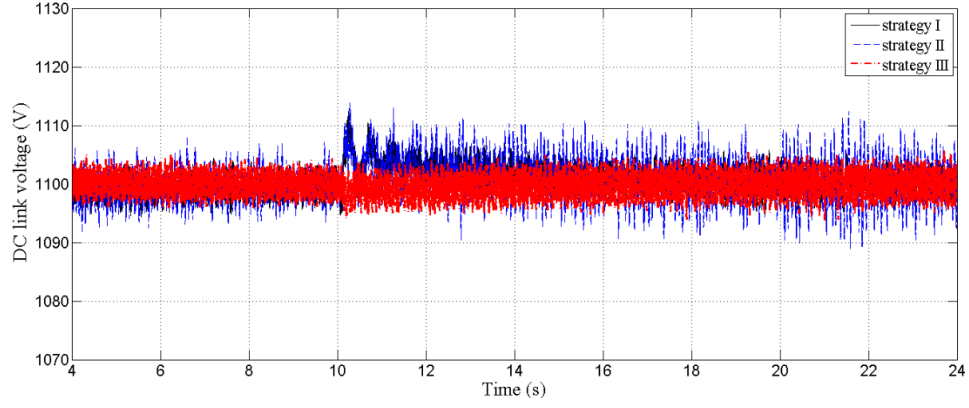
(a)



(b)

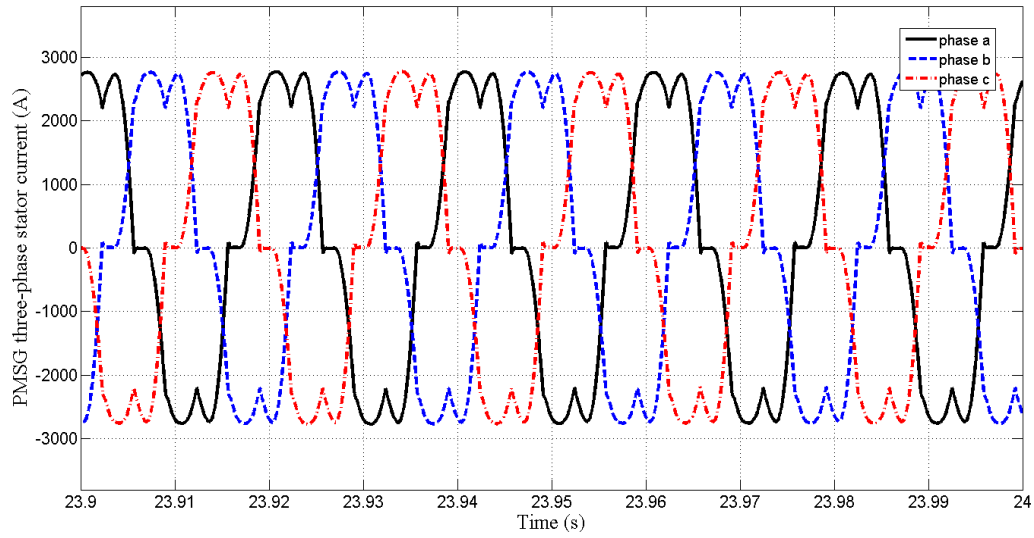


(c)

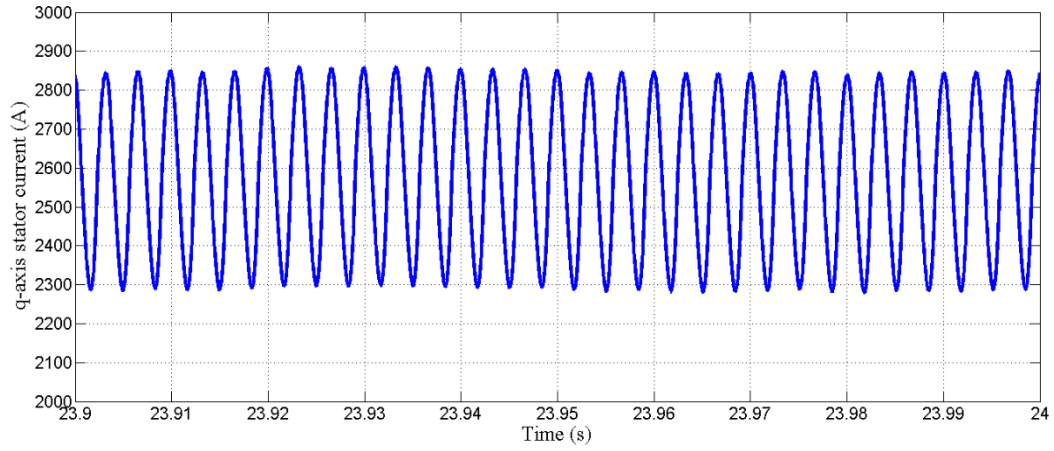


(d)

Fig. 21 System time responses with the mentioned three control strategies and against the wind speed change from 10 to 12 m/s, (a) generator speed, (b) stator active power, (c) electromagnetic torque, (d) dc-link voltage



(a)



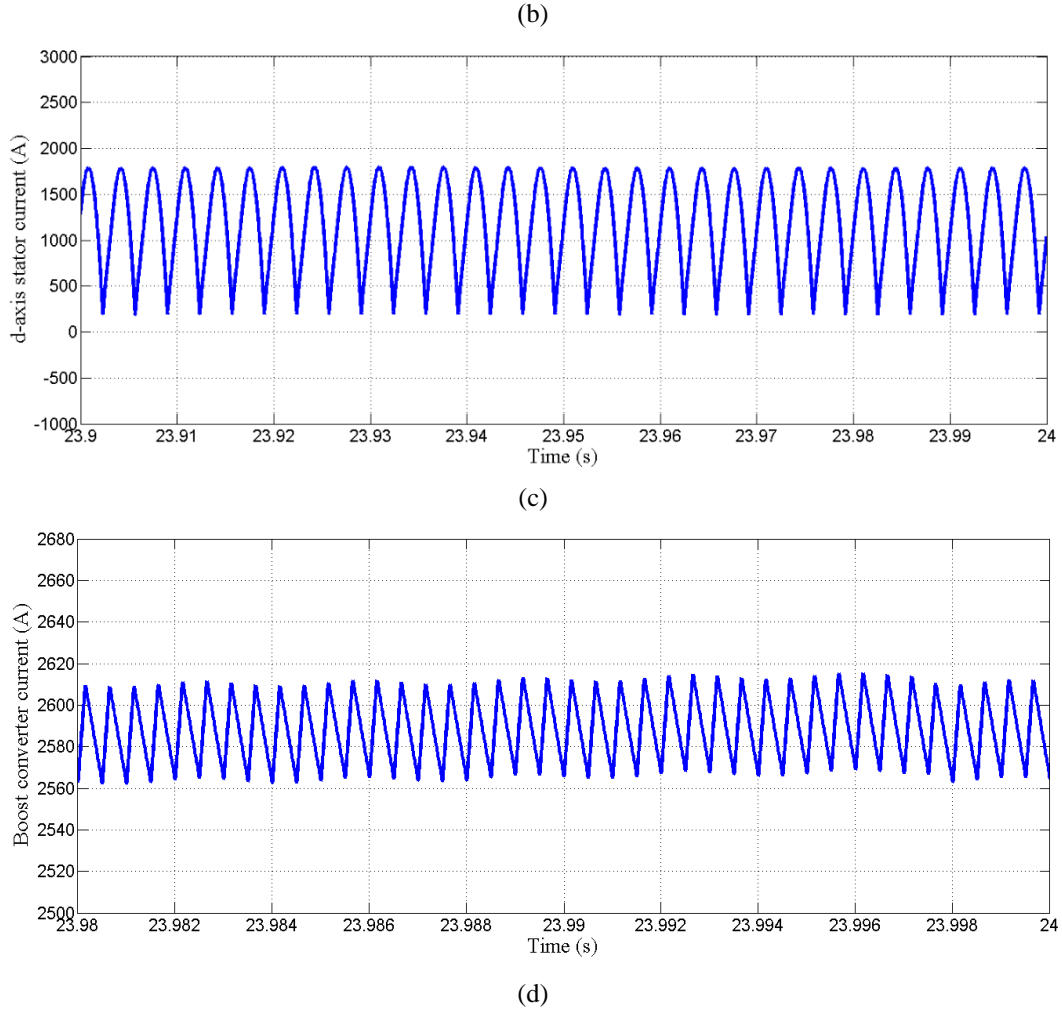
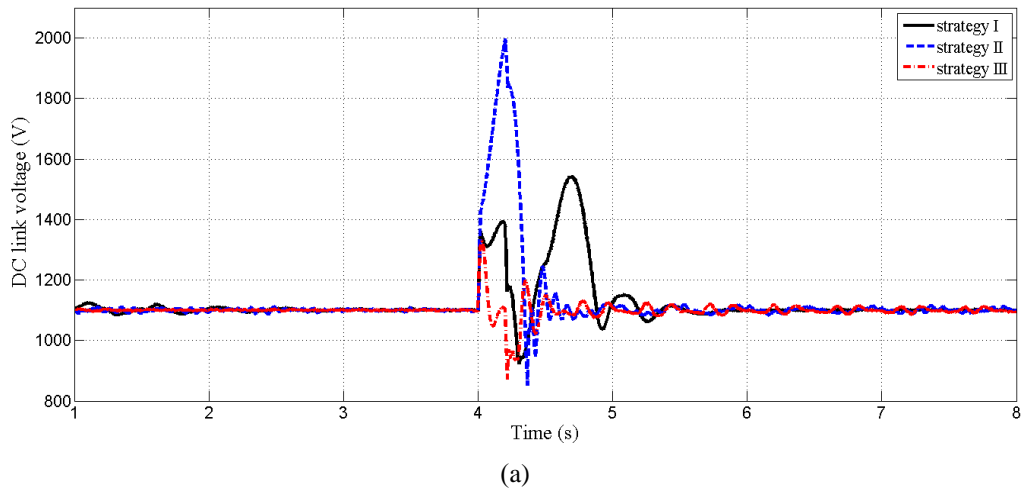
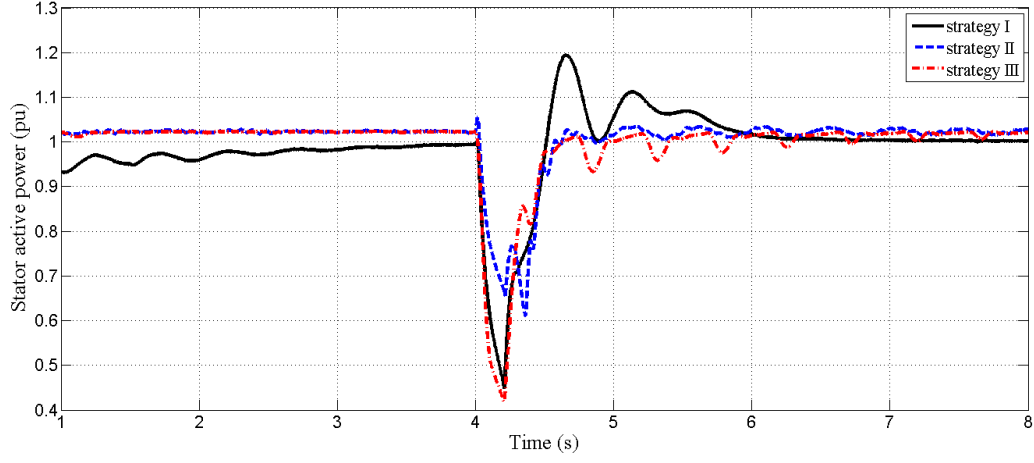
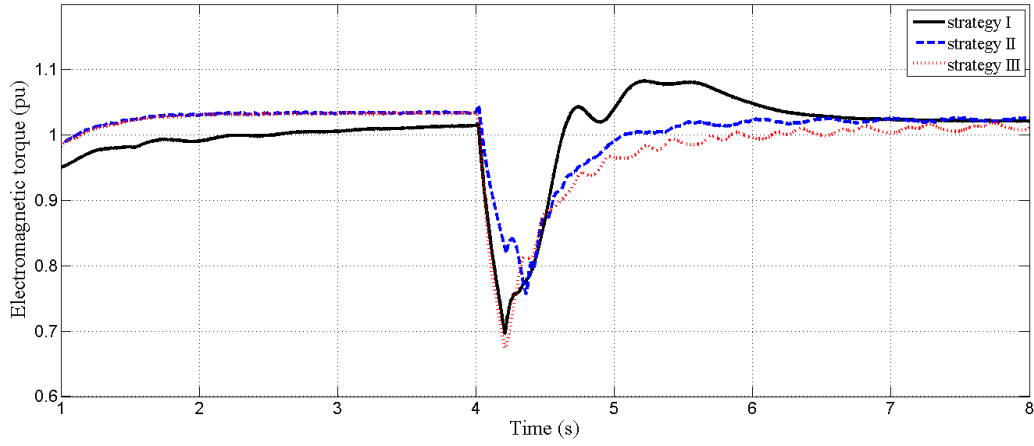


Fig. 22 Time responses of the PMSG-based WT at wind speed of 12 m/s, (a) three-phase stator current, (b) d-axis stator current, (c) q-axis stator current, (d) boost converter current

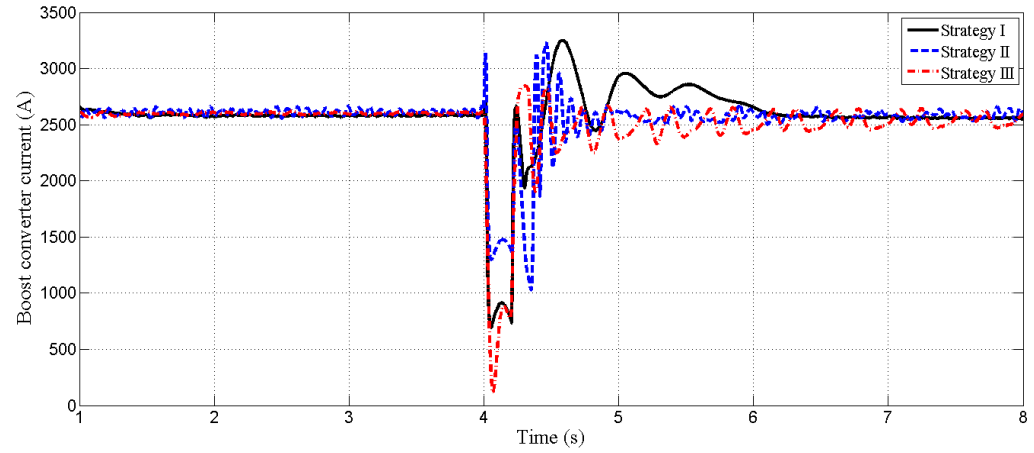




(b)

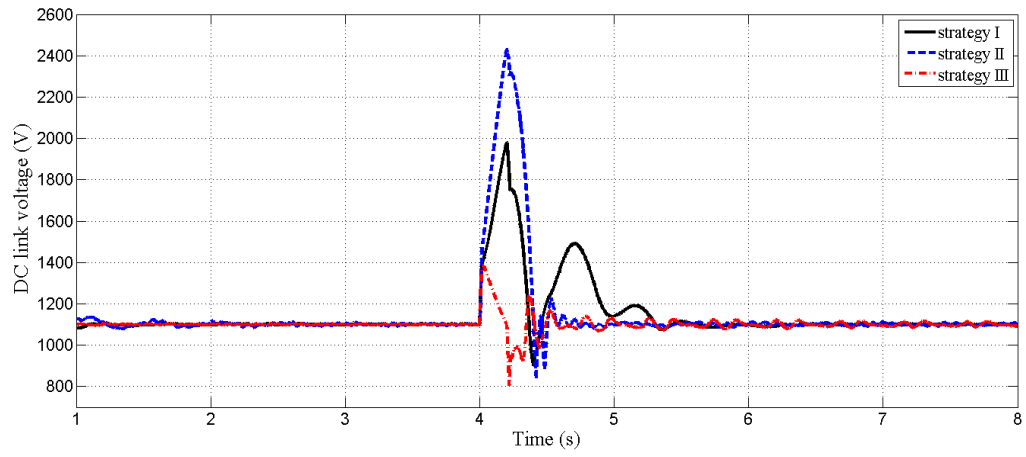


(c)

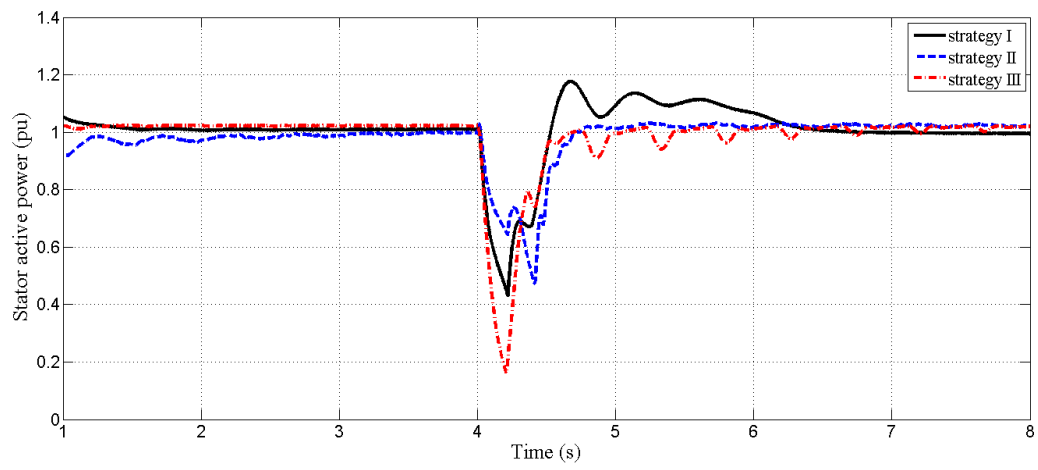


(d)

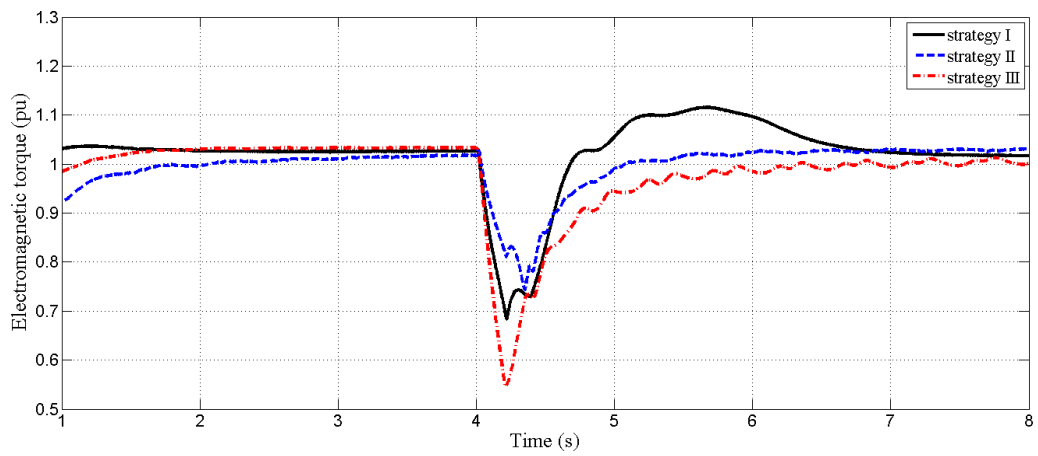
Fig. 23 System time responses with the mentioned three control strategies against 70% grid voltage dip at $t=4$ s, (a) dc-link voltage, (b) stator active power, (c) electromagnetic torque, (d) boost converter current



(a)



(b)



(c)

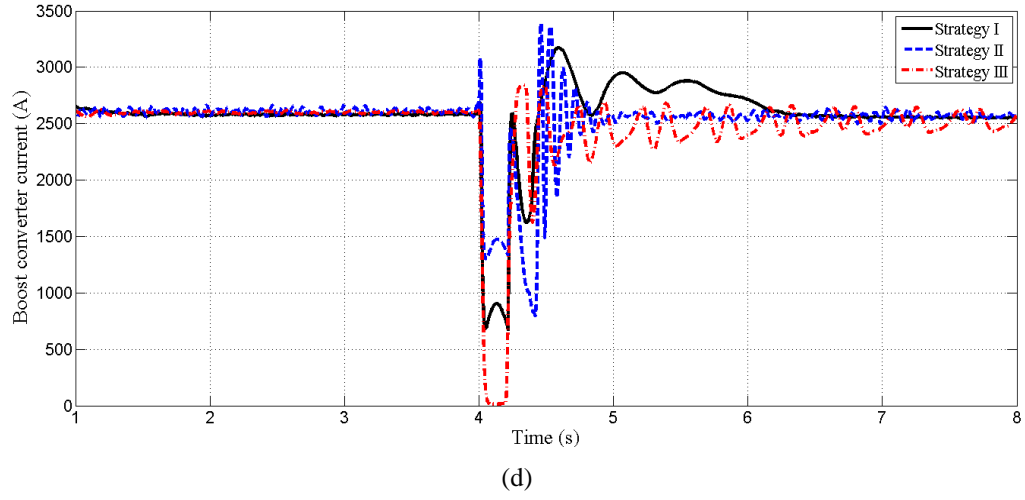


Fig. 24 System time responses with the mentioned three control strategies against 90% grid voltage dip at $t=4$ s, (a) dc-link voltage, (b) stator active power, (c) electromagnetic torque, (d) boost converter current

Table 1 Contributions of the first and second items on the average output voltage of the rectifier

Terms	Wind speed (m/s)			
	6	8	10	12
$\frac{3}{\pi} X_s i_b$	1.27	1.84	4.1	7.51
$\frac{3\sqrt{3}}{\pi} \omega_r \psi_{pm}$	132.82	158.04	208.38	259.58

Table 2 System under study parameters

Component	Parameter	Value
PMSG WT parameters	Rated Power	2 MW
	Rated stator voltage	690 v
	Rated Frequency	50 Hz
	Number of pole pairs	4
	ψ_{pm}	0.95 pu
	R_s	0.002 pu
	$L_s = L_d = L_q$	0.14 pu
	H_g, H_t	0.6 sec, 4 sec
WT transformer parameters 690 v/20 kV	X_{trans}	0.1 pu
Boost converter parameters	R_b, L_b	5 Ω , 2.4 mH
GSC parameters	DC link voltage Vdc	1100 v
	DC link capacitor Cdc	90 mF
	GSC output LC filter L_F, C_F	0.15 pu, 0.07 pu

Nomenclature:

PMSG	Permanent magnet synchronous generator (PMSG)
WT	Wind turbine
MSC	Machine side converter
GSC	Grid side converter
LVRT	Low voltage ride-through
$v_{dq}, i_{dq}, \psi_{dq}$	dq-components of the stator voltage, current and flux
ψ_{PM}	Stator flux linkage
E_g	Back-emf voltage of the stator
p, n_p	Number of generator poles and number of pole pairs
R_s, L_s, X_s	Stator resistance, synchronous inductance and synchronous reactance
T_e, ω_r	Generator torque and rotational speed
v_d, v_{dc}	Input and output voltage of boost converter
C_{dc}	DC-link capacitor
R_b, L_b	Boost converter resistance and inductance
d	Duty cycle of the boost converter switch
i_b	Boost current
$v_{GSCdq}, i_{gdq}, v_{gdq}$	dq-components of the GSC output voltage and current and grid voltage
R_f, L_f	Filter resistance and inductance
P_s, P_g	PMSG output active power and GSC output active power
H_g	Generator inertia constant

Corresponding Author: Mohsen Rahimi

Email Address: mrahimi@kashanu.ac.ir

Tel: +98(31) 55913469

Address: Department of Electrical and Computer Engineering, University of Kashan, Kashan, Iran

Biographies:

Yahya Abdollahi received his B.Sc. degree in Electrical Engineering in 2004 from Isfahan University of Technology Isfahan, Iran. He obtained the M.Sc. degree in Electrical Engineering from Shahrekord University, Shahrekord, Iran in 2011. He is currently working towards the Ph.D. degree at University of Kashan, Kashan, Iran. His research interests include power electronics, dynamic modeling and stability analysis of grid-interactive power converters, wind turbines and microgrids.

Mohsen Rahimi received his B.Sc. degree in Electrical Engineering in 2001 from Isfahan University of Technology, Isfahan, Iran. He obtained both his M.Sc. and Ph.D. degrees in Electrical Engineering from Sharif University of Technology (SUT), Tehran, Iran, in 2003 and 2011, respectively. He joined the Department of Electrical and Computer Engineering at University of Kashan, Kashan, Iran, as an Assistant Professor, in 2011. Currently, he is an Associate Professor at University of Kashan, and his major research interests include modeling and control of renewable energy sources, wind turbines and microgrids.

Abolfazl Halvaei Niasar received his B.Sc., M.Sc., and Ph.D. in 1996, 1999, and 2008 from Isfahan University of Technology (IUT), University of Tehran (UT) and Iran University of Science and Technology (IUST) all in electrical engineering respectively. He is currently with the Department of Electrical and Computer Engineering, at University of Kashan, Kashan, Iran. His research interests are mainly PM and Brushless DC motor drives, sensorless drives, design and analysis of Electrical machines, DSP based control systems and industrial control systems engineering.